14. C. W. Hoganson *et al.*, *Photosyn. Res.* **46**, 177 (1995).
15. G. T. Babcock, in *Photosynthesis: From Light to Biosphere*, P. Mathis, Ed. (Kluwer, Dordrecht, Netherlands, 1995), vol. 2, pp. 209–215.
16. _____, *et al.*, *Biochemistry* **28**, 9557 (1989).
17. G. W. Brudvig and R. H. Crabtree, *Proc. Natl. Acad. Sci. U.S.A.* **83**, 4586 (1986); J. B. Vincent and G. Christou, *Inorg. Chim. Acta* **136**, L41 (1987); V. L. Pecoraro, in *Manganese Redox Enzymes*, V. L. Pecoraro, Ed. (VCH, New York, 1992), pp. 197–231.
18. J. A. Gilbert *et al.*, *J. Am. Chem. Soc.* **107**, 3855 (1985); F. P. Rotzinger *et al.*, *ibid.* **109**, 6619 (1987); Y. Naruta, M. Sasayama, T. Sasaki, *Angew. Chem. Int. Ed.* **33**, 1839 (1994).
19. J. Messinger, M. Badger, T. Wydrzynski, *Proc. Natl. Acad. Sci. U.S.A.* **92**, 3209 (1995); J. Messinger, M. Hillier, M. Badger, T. Wydrzynski, in *Photosynthesis: From Light to Biosphere*, P. Mathis, Ed. (Kluwer, Dordrecht, Netherlands, 1995), vol. 2, pp. 283–286.
20. Kinetic inertness to substitution of the bridging oxo atoms in $Mn_2(III,IV)(\mu\text{-}O)_2$ in superoxidized manganese catalase has been suggested as the basis for inactivity of this oxidation state; G. S. Waldo, S. Yu, J. E. Penner-Hahn, *J. Am. Chem. Soc.* **114**, 5869 (1992); S. Khangulov, M. Sivaraja, V. V. Barynin, G. C. Dismukes, *Biochemistry* **32**, 4912 (1993); M. Shank, V. Barynin, G. C. Dismukes, *ibid.* **33**, 15433 (1994).
21. J. Lind, X. Shen, T. E. Eriksen, G. Merenyi, *J. Am. Chem. Soc.* **112**, 479 (1990); J. A. Kerr, in *Handbook of Chemistry and Physics* (Chemical Rubber, Cleveland, OH, ed. 77, 1996), pp. 9–51.
22. K. A. Gardner and J. M. Mayer, *Science* **269**, 1849 (1995).
23. M. Baldwin and V. L. Pecoraro, *J. Am. Chem. Soc.* **118**, 11325 (1996).
24. M. T. Caudle and V. L. Pecoraro, *ibid.* **119**, 3415 (1997).
25. M. R. A. Blomberg *et al.*, *ibid.*, in press.
26. C. K. Ingold, *Structure and Mechanism in Organic Chemistry* (Cornell Univ. Press, Ithaca, NY, ed. 2, 1969), pp. 457–463 and 681–686; A. Pross, *Theoretical and Physical Principles of Organic Reactivity* (Wiley, New York, 1995).
27. H. Koike, B. Hanssum, Y. Inoue, G. Renger, *Biochim. Biophys. Acta* **893**, 524 (1987); G. Renger and B. Hanssum, *FEBS Lett.* **299**, 28 (1992).
28. N. Lydakis-Simantiris, C. W. Hoganson, D. F. Ghanotakis, G. T. Babcock, in *Photosynthesis: From Light to Biosphere*, P. Mathis, Ed. (Kluwer, Dordrecht, Netherlands, 1995), vol. 2, pp. 279–282; N. Lydakis-Simantiris, D. F. Ghanotakis, G. T. Babcock, *Biochim. Biophys. Acta*, in press.
29. O. Bögershausen, M. Haumann, W. Junge, *Ber. Bunsenges. Phys. Chem.* **100**, 1987 (1996); M. Karge, K.-D. Irrgang, G. Renger, *Biochemistry* **36**, 8904 (1997).
30. M. Karge *et al.*, *FEBS Lett.* **378**, 140 (1996).
31. C. Tommos and G. T. Babcock, *Acct. Chem. Res.*, in press.
32. J. P. Dekker, H. J. Van Gorkom, J. Wensink, L. Ouwehand, *Biochim. Biophys. Acta* **767**, 1 (1984); J. Lavergne, *ibid.* **1060**, 175 (1991); M. Haumann, W. Drevenstedt, M. Hundelt, W. Junge, *ibid.* **1273**, 237 (1996); H. Kretschmann, E. Schlodder, H. T. Witt, *ibid.* **1274**, 1 (1996).
33. G. C. Dismukes and Y. Siderer, *Proc. Natl. Acad. Sci. U.S.A.* **78**, 274 (1981); A. Haddy, W. R. Dunham, R. H. Sands, R. Aasa, *Biochim. Biophys. Acta* **1099**, 25 (1992).
34. T. Ono *et al.*, *Science* **258**, 1335 (1992).
35. P. J. Riggs, C. F. Yocum, J. E. Penner-Hahn, R. Mei, *J. Am. Chem. Soc.* **114**, 10650 (1992).
36. T. A. Roelofs *et al.*, *Proc. Natl. Acad. Sci. U.S.A.* **93**, 3335 (1996).
37. Roeloffs *et al.* (*36*) argued against a Mn valence change on $S_2 \rightarrow S_3$, and Yachandra *et al.* (*4*) have proposed that one-electron oxidation of the bridging oxo group (or groups) occurs. However, a similar bridging oxyl ligand formulation for intermediate X in ribonucleotide reductase has been discarded recently in favor of iron-centered oxidation in the binuclear cluster in that enzyme (*58*) and the free energy necessary to generate an oxyl may be prohibitively high (*48*). Accordingly, we disfavor an oxyl formulation for S_3.
38. P. J. Riggs-Gelasco, R. Mei, C. F. Yocum, J. E. Penner-Hahn, *J. Am. Chem. Soc.* **118**, 2387 (1996); see also, J. Messinger, J. H. A. Nugent, M. C. W. Evans, *Biochemistry*, in press.
39. J.-J. Girerd, in *Photosynthesis: From Light to Biosphere*, P. Mathis, Ed. (Kluwer, Dordrecht, Netherlands, 1995), vol. 2, pp. 217–222.
40. I. Vass and S. Styring, *Biochemistry* **30**, 830 (1991).
41. X.-S. Tang *et al.*, *Proc. Natl. Acad. Sci. U.S.A.* **91**, 704 (1994).
42. K. Lindberg, T. Vänngård, L.-E. Andréasson, *Photosyn. Res.* **38**, 401 (1993).
43. K. W. Kramarz and J. R. Norton, *Prog. Inorg. Chem.* **42**, 1 (1994).
44. V. L. Pecoraro, *Photochem. Photobiol.* **48**, 249 (1988).
45. D. W. Randall *et al.*, *J. Am. Chem. Soc.* **117**, 11780 (1995).
46. F. A. Cotton and G. Wilkinson, *Advanced Inorganic Chemistry* (Wiley, New York, ed. 5, 1988), p. 707; N. N. Greenwood and A. Earnshaw, *Chemistry of the Elements* (Pergamon, Oxford, 1984), p. 1228; R. Manchandra, G. W. Brudvig, R. H. Crabtree, *Coord. Chem. Rev.* **144**, 1 (1995).
47. T. J. Collins, R. D. Powell, C. Slebodnick, E. S. Uffelman, *J. Am. Chem. Soc.* **112**, 899 (1990); M. K. Stern and J. T. Groves, in *Manganese Redox Enzymes*, V. L. Pecoraro, Ed. (VCH, New York, 1992), pp. 233–259.
48. D. T. Sawyer, *Oxygen Chemistry*, (Oxford Univ. Press, New York, 1991).
49. A. Chu, A. P. Nguyen, R. J. Debus, *Biochemistry* **34**, 5859 (1995).
50. C. W. Hoganson and G. T. Babcock, in *Metal Ions in Biological Systems*, vol. 30, *Metalloenzymes Involving Amino Acid-Residue and Related Radicals*, H. Sigel and A. Sigel, Eds., (Dekker, New York, 1994), pp. 77–107.
51. W. H. Saunders Jr. and A. F. Cockerill, *Mechanisms of Elimination Reactions* (Wiley, New York, 1973).
52. G. T. Babcock, R. E. Blankenship, K. Sauer, *FEBS Lett.* **61**, 286 (1976); M. R. Razeghifarad, C. Klughammer, R. J. Pace, *Biochemistry* **36**, 86 (1997).
53. A. Boussac, P. Sétif, A. W. Rutherford, *Biochemistry* **31**, 1224 (1992).
54. L. I. Krishtalik, *Bioelectrochem. Bioenerg.* **23**, 249 (1990).
55. G. Tian, J. A. Berry, J. P. Klinman, *Biochemistry* **33**, 226 (1994); J. P. Klinman, *Chem. Rev.* **96**, 2541 (1996).
56. R. M. Wachter and B. P. Branchaud, *J. Am. Chem. Soc.* **118**, 2782 (1996).
57. C. F. Yocum, *Biochim. Biophys. Acta* **1059**, 1 (1991); H. Wincencjusz, H. J. van Gorkom, C. F. Yocum, *Biochemistry* **36**, 3663 (1997).
58. B. E. Sturgeon *et al.*, *J. Am. Chem. Soc.* **118**, 7551 (1996).
59. Supported by NIH grant GM-37300 and the USDA Competitive Grants Office. We thank C. F. Yocum, C. Tommos, K. Warncke, N. Lydakis-Simantiris and M. Gardner for useful discussions.

26 October 1996; accepted 28 May 1997

RESEARCH ARTICLE

Global Sea Floor Topography from Satellite Altimetry and Ship Depth Soundings

Walter H. F. Smith* and David T. Sandwell

A digital bathymetric map of the oceans with a horizontal resolution of 1 to 12 kilometers was derived by combining available depth soundings with high-resolution marine gravity information from the Geosat and ERS-1 spacecraft. Previous global bathymetric maps lacked features such as the 1600-kilometer-long Foundation Seamounts chain in the South Pacific. This map shows relations among the distributions of depth, sea floor area, and sea floor age that do not fit the predictions of deterministic models of subsidence due to lithosphere cooling but may be explained by a stochastic model in which randomly distributed reheating events warm the lithosphere and raise the ocean floor.

Knowledge of ocean floor topography data is essential for understanding physical oceanography, marine biology, chemistry, and geology. Currents, tides, mixing, and upwelling of nutrient-rich water are all influenced by topography. Seamounts may be particularly important in mixing and tidal dissipation (*1*), and deep water fisheries on seamount flanks have become economically significant (*2*). Seamounts, oceanic plateaus, and other geologic structures associated with intraplate volcanism, plate boundary processes, and the cooling and subsidence of the oceanic lithosphere should all be manifest in accurate bathymetric maps.

Conventional sea floor mapping is a tedious process. Ships have measured depth with single-beam echo sounders since the

W. H. F. Smith is at the National Oceanic and Atmospheric Administration, Code E/OC-2, 1315 East-West Highway, Silver Spring, MD 20910–3282, USA.
D. T. Sandwell is at the Scripps Institution of Oceanography, La Jolla, CA 92093, USA.

*To whom correspondence should be addressed. E-mail: walter@amos.grdl.noaa.gov

Downloaded from http://science.sciencemag.org/ on January 21, 2017

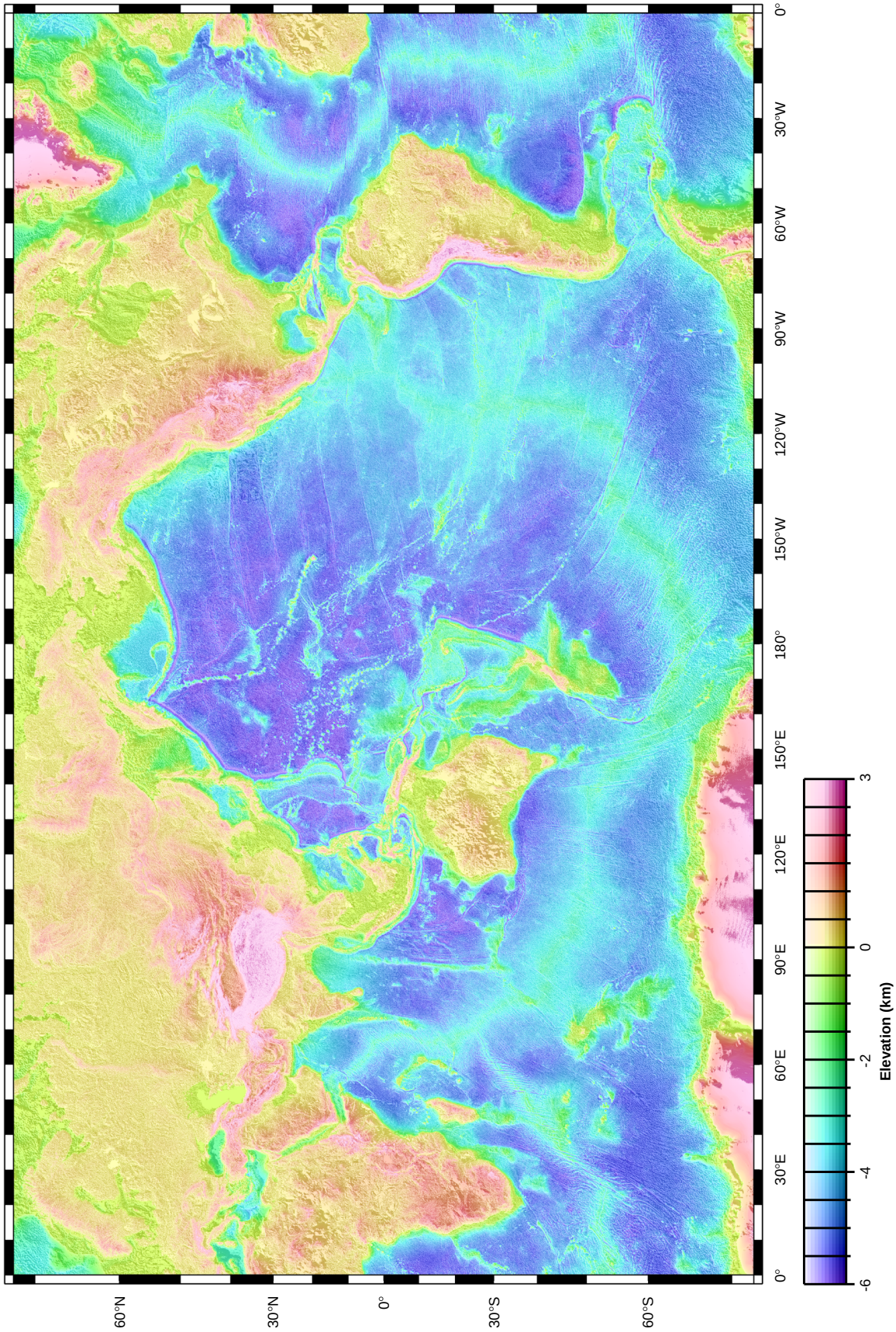

Fig. 1. Color shaded-relief image of the modeled topography, illuminated from the northwest.

Downloaded from http://science.sciencemag.org/ on January 21, 2017

1950s, but these data are sparsely distributed (hundreds of kilometers between surveys) and may have large errors in navigation and digitization (*3*). More accurate multibeam swath-mapping systems came into use on some ships in the 1980s, but in the deep ocean, these were deployed primarily along mid-ocean ridges (*4*). Some surveys are classified as secret in military archives (*5*) or remain proprietary for economic or political reasons. Global bathymetric mapping requires some means of combining these heterogeneous soundings and estimating depths in the regions where survey data are sparse. Traditionally, bathymetric contours have been drawn by hand so that intuition (or prejudice) fills the gaps in coverage. The contours may then be digitized and interpolated to produce gridded estimates. The last global syntheses were made in the late 1970s and early 1980s, yielding the fifth edition of the General Bathymetric Charts of the Oceans (GEBCO) (*6*) and the Earth Topography 5-arc-min grid (ETOPO-5) (*7*).

Recent developments allow another approach to this problem. International cooperation has yielded access to a greater variety of sounding data (*4*, *6*, *8*), and automated quality control (*3*, *9*) and archiving (*10*) methods have been devised. In addition, the ERS-1 and Geosat spacecrafts have surveyed the gravity field over nearly all of the world's ocean areas (*11*, *12*). Over the 15- to 200-km wavelength band, marine gravity anomalies are caused primarily by topographic variations on the ocean floor; thus, in principle, satellite gravity data can be used to infer some aspects of the ocean's depths. However, the topography/gravity ratio varies from one region to another because of changes in sediment thickness and other factors, so that the estimation of topography from gravity is not straightforward and requires accurate depth soundings for calibration. Here, we report our efforts to combine quality-controlled ship depth soundings with interpolation guided by satellite-derived gravity data to yield a high-resolution grid of sea floor topography.

We assembled digital depth soundings from the U.S. National Geophysical Data Center (NGDC) (*8*), the Scripps Institution of Oceanography (SIO) (*13*), and two databases derived from data originally archived at the Lamont Doherty Earth Observatory (LDEO) (*3*, *9*, *14*). Although the four sources have many cruises in common, each has unique strengths (*15*). We also obtained recent survey data directly from various investigators (*16*). Global gridded gravity anomaly data were derived from satellite altimeter measurements of sea surface slope (*11*, *17*). The accuracy of the gravity grid is 3 to 7 mgal (1 milli-Galileo = 10^{-5} m/s^2) with a resolution limit of 20 to 25 km, depending on factors such as local sea state and proximity to areas of high mesoscale ocean variability (*11*, *18*). Land elevation and shoreline data (*19*) furnished additional constraints in nearshore areas.

Method and limitations. Dixon *et al.* (*20*) have summarized the basic theory for estimating sea floor topography from gravity anomalies. Models of the isostatic compensation of sea floor topography furnish a spectral transfer function that predicts the gravity anomaly expected from sea floor topography (*21*). This transfer function is isotropic and depends on mean depth, crustal density and thickness, and elastic lithosphere thickness, and although its inverse provides a theoretical basis for estimating sea floor topography from observed gravity anomalies, there are a number of complications that require careful treatment (*20*, *22*–*25*). (i) The estimation must be restricted to a limited wavelength band, because the gravity-to-topography transfer function becomes singular at wavelengths much longer than the flexural wavelength of the lithosphere and also at wavelengths much shorter than $2\pi \times$ the mean depth, because of isostatic compensation and upward continuation, respectively. (ii) At short wavelengths, the transfer function depends on well-constrained parameters (mean depth and crustal density), but at longer wavelengths, it also depends on more variable and less certain parameters (elastic lithosphere thickness or crustal thickness). (iii) Sedimentation preferentially fills bathymetric lows and can eventually bury the original topography, adding a spatially dependent and nonlinear aspect to the transfer function. (iv) The transfer function is two dimensional and so requires complete coverage of gravity data. (v) The transfer function is nonlinear (*22*) in areas of high-amplitude topography, especially where summits approach the sea surface.

Our method uses a Gaussian filter with a half-amplitude at 160-km wavelength to smoothly separate the topography into two bands: a long-wavelength regional topography, where the transfer function requires an

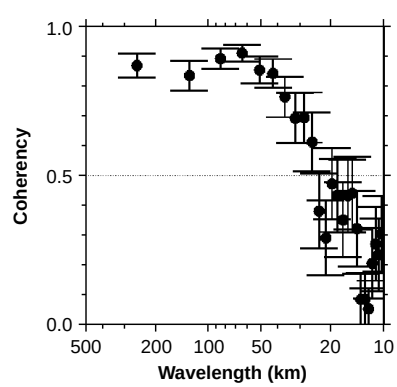

Fig. 2. Coherency between our depth estimates and the *Atalante* measurements as a function of wavelength, with one sigma error bars. Coherency values of 1, 0, and 0.5 correspond to perfect correlation, complete absence of correlation, and equal magnitudes of correlated and uncorrelated components, respectively.

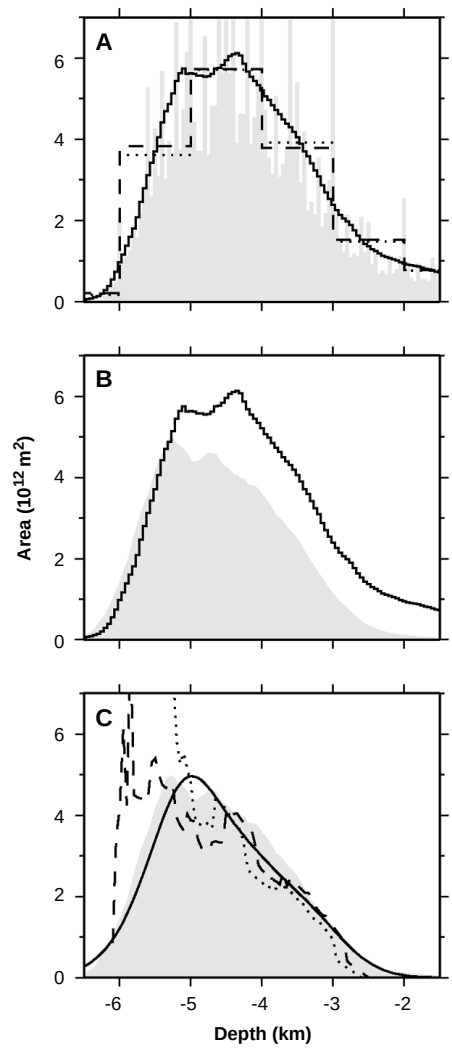

Fig. 3. Hypsometric diagrams showing sea floor area per 50-m interval of depth, as a function of depth. (**A**) Using all data. Our solution (solid line) smoothly resolves 50-m intervals, whereas ETOPO-5 (*7*) (gray bars) is biased toward contour values. Previous estimates (*34*) (dashed line) gave only 1-km intervals. Our solution for 1-km intervals (dotted line) has less area in the 5- to 6-km bin and more area in the 3 to 4-km bin than previously found, because the satellite gravity reveals more seamounts. (**B**) Solution from all data [solid line, same as in (A)] and from a restricted data set corrected for sediment thickness (gray area). (**C**) Observed hypsometry of the restricted data set [gray area, same as in (B)] and predictions of three model curves: plate models PS (*45*) (dashed line) and GDH1 (*47*) (dotted line) and our model (solid line).

Downloaded from http://science.sciencemag.org/ on January 21, 2017

assumed elastic thickness, and a short-wavelength local topography, where the transfer function is independent of the elastic thickness. We restricted gravity-derived estimation to the shorter wavelength band (*26*). We regionally calibrated the topography/gravity ratio using the local topography at points constrained by soundings, to adjust the transfer function for the effects of regionally varying sediment thickness. Our earlier method (*23*) was improved by adding a constraint-propagation step: grid cells constrained by data were set to the median of data values in the cell, and then a finite-difference interpolation routine (*27*) was used to perturb neighboring estimated values toward the constrained values. Thus, in well-surveyed areas, the accuracy and resolution depended only on the grid spacing (*17*) and the quality of the constraints and not on the gravity data. Constrained and estimated values were separately encoded so that they could be distinguished. During our process, inaccurate ship soundings became evident that were not detectable in initial quality control (*3*); these soundings were deleted from the databases, and a new estimate was made. This approach differed from another solution (*24*) in several respects (*28*).

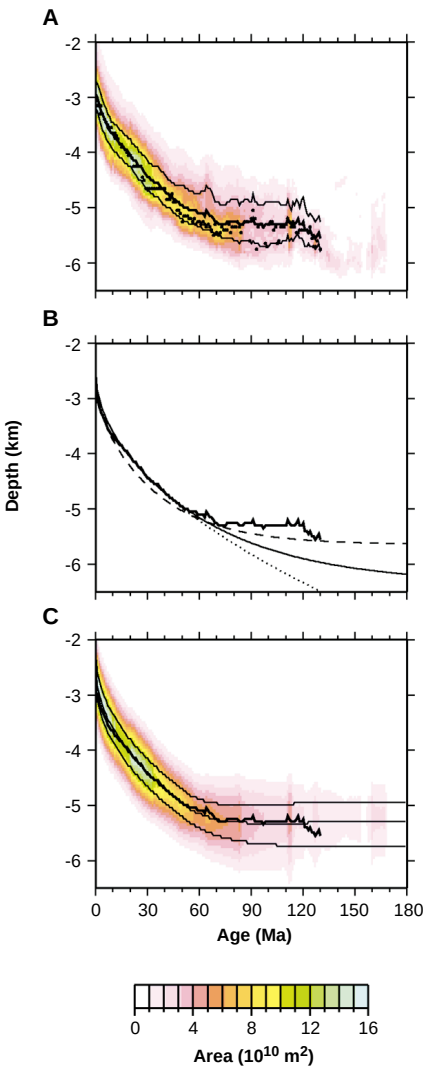

Fig. 4. Sediment-corrected depth as a function of sea floor age. (**A**) Area of the sea floor in 50-m depth and 1-My age intervals (colors, scale at bottom). Upper and lower quartiles of depth (thin lines), median depth (heavy line), and modal depth (dots) are shown in each age interval from 0 to 130 Ma, where they are reliably determined. (**B**) Observed median depth [heavy line, same as in (A)] and depth predicted by deterministic models PS (*45*) (thin solid line), GDH1 (*47*) (dashed line), and BL (*46*) (dotted line). (**C**) Synthetic data predicted by our model give an area distribution (colors, scale at bottom) and a median and quartiles of depth at each age (thin lines); the observed median [heavy line, same as in (A) and (B)] is shown for comparison.

Results, verification, and assessment. Our topography (*29*) reveals all of the intermediate- and large-scale structures of the ocean basins (Fig. 1). Incised canyons are seen in the continental margins. Spreading ridges stand out as broad highs with an axial valley along the Mid-Atlantic Ridge and an axial high along the East Pacific Rise and the Pacific-Antarctic Rise. Fracture zones reflect the direction of opening of the Atlantic basin, whereas in the Pacific they record a more complex history of major plate reorganizations. Numerous seamounts, some in linear chains, display a variety of patterns of volcanism.

We tested the precision and resolution of our estimates in a worst case scenario: a high-relief area lying more than 160 km from most soundings. After making a topography estimate, we obtained depths measured by the research vessel (R/V) *Atalante* (*30*) in a remote area of the South Pacific near the Foundation Seamounts (*31–33*). *Atalante* found seamounts with summits less than 1 km from the surface and a 6500-m-deep trough in this area, where the ocean floor typically lies at 4-km depth. The root-mean-square (rms) amplitude of these topographic variations was 791 m, whereas the rms difference between our estimates and the observed values was 250 m; thus, the estimates recovered nearly 70% of the signal. Cross-spectral coherency (Fig. 2) shows high correlation between our estimates and the observed depths at all wavelengths greater than 25 km, with a slight decrease at wavelengths greater than 100 km, where the estimation relied on interpolated soundings more than altimetry. The low coherency at wavelengths less than 25 km means that in the estimated topography, two narrow objects may blur into one object if they are closer than 12.5 km apart and objects much narrower than 12.5 km will be poorly resolved.

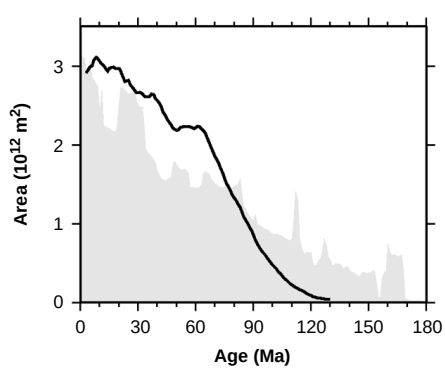

Fig. 5. Sea floor area of the sediment-corrected data set as a function of age. The gray pattern shows the relation obtained from actual sea floor age t_m. The solid line shows synthetic relation obtained from hypsometric curve by converting actual depth to thermal age t_e with the use of the BL model.

The Foundation Seamounts were unknown until they were revealed by satellite altimetry (*33*). We compared the *Atalante* depths with ETOPO-5 depths to assess how much information was missing in older maps; the (rms) difference between the two was 580 m, more than 70% of the signal. Uncharted seamounts were a significant source of topographic variation, and information from satellite gravity can reduce the error in estimated topographic variation by more than half.

Hypsometry and thermal subsidence models. Various estimates of the distribution of ocean floor area with depth, called hypsometric curves, are shown in Fig. 3A. Previous curves (*34*) were calculated in 1-km intervals. The ETOPO-5 data cannot yield a more detailed curve because of biases toward multiples of 100, 200, and 500 m, the contours that were digitized to produce ETOPO-5. Our solution yielded a smooth curve at 50-m intervals. Viewed in 1-km intervals, our solution had more area in the 3- to 4-km range and less in the 5- to 6-km range than was seen previously, reflecting the increased number of seamounts mapped by satellite altimetry (*35*).

We interpolated ages (*36*) and sediment thicknesses (*37*) to our depth grids, excluded anomalous or problematic areas (*38*) but not thermal swells, and isostatically corrected the depths in the remaining areas for the sediment load using an average sediment density (*39*). Grouping the areas of the remaining data into intervals of 50 m of depth and 1 million years (My) of age shows the variation of depth with age (Fig. 4A). These exclusions and corrections affected the hypsometry (Fig. 3B); the sediment correction slightly increased the area deeper than 5.2 km, whereas the exclusions reduced the area elsewhere. The area reduction was roughly independent of depth at

Downloaded from http://science.sciencemag.org/ on January 21, 2017

depths less than 3.5 km. There is an overall decrease of area with age, as expected if spreading ridges generate area at a constant rate, whereas subduction zones consume area independently of age (Fig. 5) (*40*). Superimposed on this are steplike changes that primarily reflect variations in spreading rate but are also caused by our exclusions of some areas (*41*). It appears that a large area of sea floor was generated during the 20 to 33 million years ago (Ma) period, implying more rapid sea floor generation with a consequent rise in sea level (*42*) and a change in global carbon chemistry (*43*).

From the distribution of area with depth within each age interval, we found the modal depth, the median depth, the first and third quartile depths, and the interquartile range (IQR) (*44*) (Fig. 4A). The mode and quantiles deepened with age from 0 to 55 Ma and then abruptly flatten and become nearly constant at ages older than 70 Ma. Comparing these statistics with the area distribution (Fig. 4A) shows that in every age interval the distribution of depths is skewed, with more area above the mode than below it. Seamounts would cause this. The IQR was about 0.5 km for the first 27 My, increased to 0.75 km at 80 Ma, and stayed nearly constant at older ages. These statistics are not reliably determined at ages older than 130 Ma because the available sample of area is small.

Thermal models of the cooling and subsidence of oceanic lithosphere (*45*) predict that depth z should increase monotonically with the age of the sea floor t as the lithospheric plate moves away from the hot mid-ocean ridge where it formed. Because these models treat z deterministically, they will not explain why the variation we observe in z increases with t, and we therefore compare them with the median z at each t. The simplest model is the "boundary layer" (BL) model (*46*), which predicts that z should increase with t according to

$$z(t) = r + a\sqrt{t} \tag{1}$$

where $r = 2.5$ km is the depth at zero age and $a = 0.35$ km/(My)$^{1/2}$ is the subsidence rate. This model gives a good fit to the median depths (Fig. 4B) in the 0 to 55 Ma age range, but not beyond that, where the observed depths flatten. A model that imitates BL for a time and then flattens is the "plate model," which predicts that

$$z(t) = r + h\left\{1 - \frac{8}{\pi^2} \times \sum_{n=1}^{\infty} \frac{1}{(2n+1)^2} \exp[-n^2 t/\tau]\right\} \tag{2}$$

in which h is the overall subsidence from zero to infinite age and τ is a characteristic time. For $t < \tau$, Eq. 2 gives approximately the same behavior as Eq. 1 with $a = 4h/\pi^3\tau$, whereas for larger t, the $z(t)$ curve will flatten. A plate model with r and a as in BL and $\tau = 62.8$ My, we call model "PS" after its authors (*45*); a model with $r = 2.6$ km, $a = 0.365$ km/(My)$^{1/2}$, and $\tau = 36$ My was called "Global Depth and Heat Flow 1" or GDH1 by its authors (*47*). Model PS fits the median depths in the same range as model BL (Fig. 4B) because it has the same initial behavior; it also begins to flatten at about the right time. However, the flattening is not abrupt enough to fit the data. Model GDH1 achieves greater flattening by using a smaller τ than model PS, but to have approximately the right overall subsidence h, GDH1 increases a to compensate for the decreased τ; this causes it to predict too much initial subsidence and a too early onset of flattening while still failing to follow the abrupt flattening observed. Hypsometric curves predicted by models PS and GDH1 (*48*) (Fig. 3C) are not a good match to the observations; they imitate the variations in the area-age distribution too closely, they predict less area than is observed at depths shallower than 5000 m, and they predict that large areas of the ocean floor should lie at the asymptotic depth of the model.

We propose a stochastic reheating model to explain the hypsometry, the abrupt flattening of median depth with age, and the increased variability of depth at older ages. It is based on the following observations: (i) different regions in the oceans subside like BL until different flattening ages, some as old as 170 Ma (*49*); (ii) depth and heat flow in some old basins behave like BL but with an effective thermal age t_e, which is younger than the (paleomagnetically determined) actual age t_m (*50*); (iii) effective elastic lithosphere thicknesses under some intraplate volcanoes suggest that hot spots produce a "thermal rejuvenation," reducing t_e (*51*); (iv) the depths and subsidence of hot spot swells suggest that many swells reduce t_e to the same value (*52*); and (v) on old lithosphere, it is hard to find areas that have not been near hot spots (*53*). If N sites of reheating, each affecting an area of diameter D, are uniformly and randomly distributed in an area A_h, and the plates making up A_h move over these sites with velocity V, then in a steady-state situation with A_h, D, N, and V all independent of time, the probability density function $p(t)$ for t, the time since any point's last reheating, is

$$p(t) = \frac{1}{\alpha}\exp[-t/\alpha] \tag{3}$$

where

$$\alpha = A_h/NDV \tag{4}$$

is the mean time between reheating events (*54*). If reheating events always reset t_e to a fixed value t_0, whereas lithosphere younger than t_0 is not affected by reheating, and if the sea floor we observe is a random sample from such a system, then χ, the chance that sea floor of (actual) age t_m has not been reheated since t_0, is

$$\chi(t_m) = \begin{Bmatrix} 1 & \text{if } t_m \le t_0 \\ \exp[-(t_m - t_0)/\alpha] & \text{if } t_m > t_0 \end{Bmatrix} \tag{5}$$

and the probability density function for t_e given an observed t_m is

$$p(t_e|t_m) = \begin{Bmatrix} \delta(t_e - t_m) & \text{if } t_m \le t_0 \\ \chi(t_m)\delta(t_e - t_m) + \frac{1}{\alpha}\exp\left[\frac{-(t_e - t_0)}{\alpha}\right] & \text{if } t_0 \le t_e \le t_m \end{Bmatrix} \tag{6}$$

This model predicts that (i) when $t_m \le t_0$, t_e is deterministic and $t_e = t_m$; (ii) as t_m exceeds t_0, a fraction $(1 - \chi)$ of the area has $t_e < t_m$; (iii) when $t_m > t_0 + \alpha \log 2$, the median t_e is less than t_m; and (iv) at large t_m, $\chi \to 0$ and a steady state prevails in which t_e is independent of t_m. In the steady state, the mean effective age is $\mu_t = t_0 + \alpha$ and the standard deviation of the effective ages is $\sigma_t = \alpha$.

If z follows the BL cooling rule with t_e in Eq. 1, then the probability density for z given t_m is

$$p(z|t_m) = \begin{Bmatrix} \delta(z - z_m) & \text{if } t_m \le t_0 \\ \chi(t_m)\delta(z - z_m) + f(z) & \text{if } t_m > t_0 \end{Bmatrix} \tag{7}$$

where

$$f(z) = \begin{Bmatrix} 0 & z \notin (z_0, z_m) \\ \frac{2(z - r)}{a^2\alpha} \times \exp\left\{\frac{-[(z - r)^2 - (z_0 - r)^2]}{a^2\alpha}\right\} & z \in (z_0, z_m) \end{Bmatrix} \tag{8}$$

and z_0 and z_m are the depths corresponding to t_0 and t_m in Eq. 1. The change of variables from t_e to z is nonlinear so the mean and standard deviation of z cannot be found from μ_t and σ_t; however, the quantiles (*44*) can be transformed: $z_Q = r + a\sqrt{t_Q}$ always, and $t_Q = t_0 - \alpha \log(1 - Q)$ in the steady state.

The predictions formed by our model with $t_0 = 45$ My and $\alpha = 25$ My combined with a Gaussian noise process having a zero

Downloaded from http://science.sciencemag.org/ on January 21, 2017

mean and an IQR of 0.5 km at all ages are shown in Figs. 3C and 4C. We added this noise to simulate the variability of the data at ages younger than t_0, where the model is deterministic. Taking $A_h = 115 \times 10^{12}$ m^2, the area of the sea floor older than 45 Ma, if D and V are roughly 1000 km and 80 km/My, respectively, then $\alpha = 25$ My gives $N = 57$ reheating sites in this area, and αV, the characteristic distance between reheating sites, is about 2000 km. We were able to obtain reasonable fits to the data in Figs. 3C and 4C with other values as well (for example, $t_0 = 40$ and $\alpha = 30$), but we caution against overfitting the data; the Gaussian noise, being symmetric, does not realistically simulate the skewed variability produced by seamounts.

If one merely desired to explain the hypsometry, any reheating process that converted t_m to t_e such that the distribution of area with t_e was as shown by the curve in Fig. 5 would suffice. This curve is obtained from the hypsometric curve by converting z to t_e with the inverse of Eq. 1. It shows that t_e is usually less than t_m and that areas with t_e older than 130 My are rare. Reheating that is concentrated primarily in one area (*55*) or at one age (*56*) might explain some features of the area-t_e distribution in Fig. 5, but the age independence of the depth distribution at old age (Fig. 4A) suggests a model with reheating events randomly distributed in space and time.

Boundary layer cooling is the physically expected behavior unless some other thermal process intervenes. The plate model assumes that a fixed temperature is maintained at a fixed depth everywhere and so predicts that subsidence curves should flatten at the same age everywhere; they do not (*49*). Our model indicates that from time to time some areas will probably be reheated (*57*) and uplift and rejuvenated subsidence may occur anywhere at any time after t_0. The depth at any individual site older than t_0 may be between z_0 and z_m, but the aggregate properties of a large sample of sites should have order statistics (*44*) predicted by the model; these statistics can flatten more abruptly than the plate model subsidence curve if α is small compared with τ. Old areas are rare in comparison with young areas (Fig. 5) and constitute a small sample. Thus, the fact that some sites on old sea floor have depths lying on the PS plate model curve (*45*, *50*) does not disprove our model. The heat flow at these sites argues for reheating and against the plate model (*50*).

REFERENCES AND NOTES

1. R. G. Lueck and T. M. Mudge, *Science* **276**, 1831 (1997).
2. J. A. Koslow, *Am. Sci.* **85**, 168 (1997).
3. W. H. F. Smith, *J. Geophys. Res.* **98**, 9591 (1993).
4. W. B. F. Ryan, W. Menke, D. Caress, W. F. Haxby, *RIDGE Multibeam Synthesis Project* (Lamont Doherty Earth Observatory, Columbia University, Palisades, NY, 1995).
5. Medea Committee, *Scientific Utility of Naval Environmental Data* (Mitre, McLean, VA, 1995).
6. Canadian Hydrographic Office, *General Bathymetric Chart of the Oceans (GEBCO)* (Hydrographic Chart Distribution Office, Ottawa, Canada, ed. 5, 1981). The fifth edition was the last global synthesis; newer contours in regional areas are included on the GEBCO Digital Atlas CD-ROM, available from the British Oceanographic Data Centre.
7. National Geophysical Data Center, *ETOPO-5 Bathymetry/Topography Data* (Data Announcement 88–MGG–02, National Oceanic and Atmospheric Administration, U.S. Department of Commerce, Boulder, CO, 1988). The ETOPO-5 data combine various sources of land elevation data with a Digital Bathymetric Data Base at 5 arc min produced in the early 1980s by the U.S. Naval Oceanographic Office from hand-drawn contour charts. The U.S. Navy spent 176 person-years contouring and gridding its charts (*5*). Errors in this data set are discussed in (*3*).
8. National Geophysical Data Center, *Worldwide Marine Geophysical Data TRKDAS CD-ROM version 3.1* (Data Announcement 95–MGG–02, National Oceanic and Atmospheric Administration, U.S. Department of Commerce, Boulder, CO, 1995). As the World Data Center A for Marine Geology and Geophysics, the NGDC is the world's primary archive for ship sounding data.
9. P. Wessel and A. B. Watts, *J. Geophys. Res.* **93**, 393 (1988).
10. P. Wessel and W. H. F. Smith, *Eos* **72**, 441 (1991).
11. D. T. Sandwell and W. H. F. Smith, *J. Geophys. Res.* **102**, 10039 (1997).
12. In March 1995, ERS-1 completed its mapping, and in July 1995, all of the data collected by Geosat were declassified. The ERS-1 data cover latitudes between ±81.5° along orbital tracks spaced 8 km apart at their widest point (on the equator); the Geosat data cover latitudes between ±72° on tracks 5 km apart at the equator. We combined and processed these two data sets to form a global marine gravity grid between latitudes of ±72° (*11*).
13. SIO has a reserved archive of Indian Ocean surveys by the R/V *Marion Dufresne*. M. Munschy and R. Schlich granted us use of these data, which filled an important gap in coverage.
14. S. Cande has assembled a database with quality control optimized for studies of magnetic anomalies; it includes data originally archived at LDEO plus additional cruise data in the Southern Ocean that are not available elsewhere.
15. The most reliable soundings come from the LDEO-derived databases because over time many researchers have inspected these data, corrected errors, and digitized older analog soundings. One version of the LDEO data was quality-controlled for gravity studies by Wessel (*9*) and for bathymetry by Smith (*3*). A slightly different version was assembled by Cande (*14*). The NGDC archive (*8*) has the most complete geographic coverage but has been through minimal quality control; data from it were used only where the LDEO-derived data sets lacked coverage. The SIO database was searched for cruise data that were not in the other three databases (*13*). Data from the four sources were merged into a common format at SIO with the use of the database and quality-control methods developed at LDEO by Wessel and Smith (*3*, *9*, *10*). Where multibeam surveys exist, we used only the center beam to match the format of the more common single-beam data.
16. New surveys, particularly along the Pacific-Antarctic and Southeast Indian ridges, went to previously unexplored areas and were largely guided by the satellite gravity observations; thus, they covered some of the newly discovered high-relief features in the ocean basins.
17. Our gravity (*11*) and bathymetry grids have cell dimensions of 2 min in longitude and cosine (latitude) by 2 min in latitude (Mercator projection) so that cells are equidimensional but vary in size with latitude, being 3.7 km at the equator and 1.1 km at 72°. A total of 68,428,800 cells cover the area between ±72° latitude. The gravity solution combines 4.5 years of Geosat data and 2 years of ERS-1 data. The higher accuracy profiles come from averages of 16 ERS-1 repeat cycles along its 35-day repeat orbit and up to 66 Geosat repeat cycles along its 17-day repeat orbit. The higher spatial density profiles (*12*) come from the 1.5-year Geosat Geodetic Mission and the 1-year ERS-1 Geodetic Phases I and II.
18. K. M. Marks, *Geophys. Res. Lett.* **23**, 2069 (1996).
19. We used the 30-arc-sec global land topography "GTOPO30" archived by the U.S. Geological Survey at http://edcwww.cr.usgs.gov/landdaac/gtopo30/gtopo30.html. Shorelines north of 60°S were taken from P. Wessel and W. H. F. Smith [*J. Geophys. Res.* **101**, 8741 (1996)]; these have 50-m to 5-km resolution. Shorelines south of 60°S were taken from the Scientific Committee on Antarctic Research [*Antarctic Digital Database CD-ROM* (British Antarctic Survey, Cambridge, UK, 1993)]; these come from charts at scales between 1:200,000 and 1:5,000,000.
20. T. H. Dixon, M. Naraghi, M. K. McNutt, S. M. Smith, *J. Geophys. Res.* **88**, 1563 (1983).
21. N. M. Ribe, *Geophys. J. R. Astron. Soc.* **70**, 273 (1982).
22. R. L. Parker, *ibid.* **31**, 447 (1973).
23. W. H. F. Smith and D. T. Sandwell, *J. Geophys. Res.* **99**, 21803 (1994).
24. G. Ramillien and A. Cazenave, *J. Geodyn.* **23**, 129 (1997).
25. See also N. Baudry and S. Calmant, *Geophys. Res. Lett.* **18**, 1143 (1991); W.-Y. Jung and P. R. Vogt, *Tectonophysics* **210**, 235 (1992); L. Sichoix and A. Bonneville, *Geophys. Res. Lett.* **23**, 2469 (1996); M. McNutt and A. Bonneville, *Endeavour* **20**, 157 (1996).
26. This choice is a compromise between including more gravity information in areas of widely spaced ship soundings and minimizing the errors from not knowing the spatial variations in elastic thickness. Justification of this choice and derivation of the Gaussian filter in terms of the uncertainty in elastic thickness are given in (*23*).
27. W. H. F. Smith and P. Wessel, *Geophysics* **55**, 293 (1990).
28. We started with the original sounding data rather than ETOPO-5, combined gravity data from two satellites, allowed for regional variation in sediment thickness, did not make assumptions about the elastic thickness of the lithosphere, and forced the solution to agree with measured depths and coastlines.
29. W. H. F. Smith and D. T. Sandwell, *Measured and Estimated Sea Floor Topography* (Publication RP–1, World Data Center A for Marine Geology and Geophysics, Boulder, CO, 1997). This publication is a 34" by 53" printed map available from the NGDC and SIO. The digital grid (version 6.2) is available by anonymous ftp at topex.ucsd.edu; digital images can be downloaded from http://topex.ucsd.edu/marine_topo/mar_topo.html.
30. One of us (D.T.S.) participated in this 1997 expedition, which was led by M. Maia, Chief Scientist. Depths used in this comparison are center beam values from a Simrad 12D (Kongsberg Simrad AS, Horton, Norway) multibeam system.
31. J. Mammerickx, *Earth Planet. Sci. Lett.* **113**, 293 (1992).
32. C. Devey *et al.*, *Cruise Report SO-100: The Foundation Seamount Chain* (Kiel University, Kiel, Germany, 1995).
33. The Foundation Seamounts area was poorly surveyed by ships until a 1995 expedition of the R/V *Sonne* (*32*). In 1991, Mammerickx (*31*), by visual inspection of gravity anomalies apparent in the widely spaced satellite altimeter profiles then available, inferred the existence of this 1600-km-long volcanic chain, which she named the Foundation Seamounts. When dense Geosat altimeter data south of 30°S were declassified in 1992, we refined the maps of this area using our estimation method (*23*). Our map guided the R/V *Sonne* expedition (*32*), which found 44 previously unsurveyed volcanoes with heights ranging from 1500 to 4000 m; eleven of these volca-

Downloaded from http://science.sciencemag.org/ on January 21, 2017

noes come to within 500 m of the ocean surface. In 1997, the R/V *Atalante* surveyed another part of this area (*30*), generally more than 160 km away from the *Sonne* survey. We made an initial depth estimation using the *Sonne* data and the older sparse data, but not the *Atalante* data, in order to use the latter as an independent "blind" test of our method.
34. H. W. Menard and S. M. Smith, *J. Geophys. Res.* **71**, 4305 (1966).
35. Menard and Smith (*34*) compared their solution with one obtained in 1921 and noted the same phenomenon: the newer solution found more area at shallower depths because the ability to detect seamounts had improved in the interim. Our comparison with their results was not strictly valid because they included the Arctic Ocean, whereas we worked within ±72° latitude. However, the Arctic Ocean is only 3% of the entire ocean area, and it is shallower on average; thus, adding the Arctic to our data would only increase the shallowing of our solution over theirs.
36. D. M. Müller, W. R. Roest, J.-Y. Royer, L. M. Gahagan, J. G. Sclater, *J. Geophys. Res.* **102**, 3211 (1997).
37. D. L. Divins gave us a sediment thickness grid that he is preparing for NGDC distribution.
38. Areas where sediment thickness exceeded 2 km (continental slopes and rises) were excluded because the sediment correction is complicated in areas of thick sediment; see S. Le Douaran and B. Parsons, *J. Geophys. Res.* **87**, 4715 (1982). The Bauer Microplate was excluded because the age model (*36*) may be wrong in this area. The Scotia Plate and the Marianas and Philippine back-arc basins were excluded because their depths are known to be anomalous. The following ridges, rises, banks, and plateaus were excluded because they are known to have anomalous crustal thickness: Agulhas, Azores, Chagos-Laccadive, Conrad, Del Caño, Galapagos, Hess, Iceland, Kerguelen, Line Islands, Mid-Pacific Mountains, Naturaliste, Nazca, Ninety-East, Ontong-Java, Rio Grande, Seychelles, Shatsky, Tuamotu, and Walvis.
39. M. L. Renkin and J. G. Sclater, *J. Geophys. Res.* **93**, 2919 (1988).
40. B. Parsons, *ibid.* **87**, 289 (1982).
41. The age grid (*36*) was interpolated by assuming a constant spreading rate between identifiable magnetic anomalies, hence the steplike pattern.
42. J. D. Hays and W. C. Pitman III, *Nature* **246**, 18 (1973); W. C. Pitman III, *Geol. Soc. Am. Bull.* **89**, 1389 (1978).
43. W. H. Berger and E. L. Winterer, *Int. Assoc. Sedimentol. Spec. Publ.* **1**, 11 (1974).
44. An "order statistic" or "quantile" x_Q divides a distribution of x values so that a fraction Q of them are less than x. The median is $x_{1/2}$. The first and third quartiles are the values $x_{1/4}$ and $x_{3/4}$. The IQR $= x_{3/4} - x_{1/4}$ measures the dispersion of the distribution. The mode is that value of x that occurs most frequently; here, it is the center of the 50-m interval of depth having the most area.
45. B. Parsons and J. Sclater, *J. Geophys. Res.* **82**, 803 (1977).
46. D. L. Turcotte and E. R. Oxburgh, *J. Fluid Mech.* **28**, 29 (1967); E. E. Davis and C. R. B. Lister, *Earth Planet. Sci. Lett.* **21**, 405 (1974).
47. C. A. Stein and S. Stein, *Nature* **359**, 123 (1992).
48. The hypsometric curve predicted by a plate model was found by treating the distribution of area with age as $\Delta A/\Delta t$, a discrete approximation of the rate of change of cumulative area with age, treating the hypsometric curve similarly as $\Delta A/\Delta z$, and relating the two through dz/dt, the derivative of the subsidence predicted by the plate model. This method was given in (*40*), but that paper assumed a linear function for $\Delta A/\Delta t$, whereas we used the actual data (gray area of Fig. 5).
49. J. C. Marty and A. Cazenave, *Earth Planet. Sci. Lett.* **94**, 301 (1989).
50. S. Nagihara, C. R. B. Lister, J. G. Sclater, *ibid.* **139**, 91 (1996).
51. H. W. Menard and M. K. McNutt, *J. Geophys. Res.* **87**, 8570 (1982); M. K. McNutt, *ibid.* **89**, 11180 (1984); W. H. F. Smith, H. Staudigel, A. B. Watts, M. S. Pringle, *ibid.* **94**, 10501 (1989).
52. S. T. Crough, *Geophys. J. R. Astron. Soc.* **55**, 451 (1978).
53. R. L. Heestand and S. T. Crough, *J. Geophys. Res.* **86**, 6107 (1981).
54. S. T. Crough, *Tectonophysics* **61**, 321 (1979).
55. S. Calmant and A. Cazenave, *Nature* **328**, 236 (1987); M. K. McNutt and K. Fischer, *Geophys. Monogr. Am. Geophys. Union* **43**, 25 (1987).
56. R. L. Larson, *Sci. Am.* **272**, 82 (February 1995).
57. If the thermal diffusivity and thermal expansivity are constant, then depth is proportional to the integral of temperature over the lithosphere (*45*, *46*). Any reheating mechanism that resets the effective thermal age, as sensed by depth, will do; several of these mechanisms are discussed in (*50*).
58. This work was supported primarily by NSF Ocean Sciences grant OCE95-21518, with some additional support from NASA Solid Earth and Natural Hazards grant NAGW3035. We thank the many scientists who provided us with soundings from their recent cruises.

8 April 1997; accepted 5 August 1997

Location, Location, Location...

Discover three indispensable World Wide Web services exclusively from SCIENCE at one easy to find location:

- SCIENCE Online, including the SCIENCE Table of Contents and fully searchable database research abstracts and news summaries.
- SCIENCE Classified Advertising Online
- SCIENCE Electronic Marketplace

Discover a whole new world of SCIENCE at the location below.

www.sciencemag.org

SCIENCE

Downloaded from http://science.sciencemag.org/ on January 21, 2017

EXTENDED PDF FORMAT
SPONSORED BY

www.rndsystems.com

Science
AAAS

Global Sea Floor Topography from Satellite Altimetry and Ship Depth Soundings

Walter H. F. Smith and David T. Sandwell (September 26, 1997)
Science **277** (5334), 1956-1962. [doi: 10.1126/science.277.5334.1956]

Editor's Summary

This copy is for your personal, non-commercial use only.

Article Tools Visit the online version of this article to access the personalization and article tools:
http://science.sciencemag.org/content/277/5334/1956

Permissions Obtain information about reproducing this article:
http://www.sciencemag.org/about/permissions.dtl

Science (print ISSN 0036-8075; online ISSN 1095-9203) is published weekly, except the last week in December, by the American Association for the Advancement of Science, 1200 New York Avenue NW, Washington, DC 20005. Copyright 2016 by the American Association for the Advancement of Science; all rights reserved. The title *Science* is a registered trademark of AAAS.

Downloaded from http://science.sciencemag.org/ on January 21, 2017